Self-assembled patterns and strain-induced instabilities for modulated systems

Eliana Asciutto, Christopher Roland, and Celeste Sagui
Center for High Performance Simulations and Department of Physics, The North Carolina State University, Raleigh, North Carolina 27695-8202 USA
(Received 24 February 2005; published 15 August 2005)

The self-assembled domain patterns of modulated systems are characteristic of a wide variety of chemical and physical systems, and are the result of competing interactions. From a technological point of view, there is considerable interest in these domain patterns, as they form suitable templates for the fabrication of nanostructures. We have analyzed the domains and instabilities that form in modulated systems, and show that a large variety of patterns—based on long-lived *metastable* or *glassy* states—may be formed as a compromise between the required equilibrium modulation period and the *strain* present in the system. The strain results from topologically constrained trajectories in phase space, that effectively preclude the equilibrium configuration.

DOI: 10.1103/PhysRevE.72.021504 PACS number(s): 64.75.+g, 61.20.Ja, 75.70.Kw

I. INTRODUCTION

The kinetics of first-order phase transitions are characterized by a high degree of universality, such that a large variety of materials systems display the same kinds of structural motifs and dynamical ordering mechanisms, albeit on very different length and time scales [1]. This is irrespective of the underlying microscopic interactions responsible for the ordering, which indeed may be very different. Universal features are particularly striking in *modulated systems*, which are characterized by *effective short-range attractive* and *long-range repulsive* interactions (LRRI) [2,3]. Here, the interactions conspire to produce patterns based on lamellar "stripe" and circular "bubble" motifs in two dimensions, and spheres, tubes, and sheets in three dimensions. Examples of systems characterized by modulated phases abound in nature, and include prototypical examples such as magnetic garnet films [4–16], ferromagnetic surface layers [17], ferro- and dielectric fluids [18–20], ferroelectrics [21,22], Langmuir monolayers [23–28], block-copolymer systems [29,30], liquid crystal systems [31–34], charged colloidal suspensions [35–37], lipids and corresponding membranes and vesicles [38–42], type I superconductors [43–45], steady-state reaction-diffusion (Turing) patterns [46], Swift-Hohenberg fluid systems [47–49], surface science systems [50,51], and the primate visual cortex [52].

Understanding the time evolution of modulated systems has been a problem of long lasting interest and importance. Recently, there has been a resurgence of interest in this issue, brought about by the advent of nanotechnology [53,54]. It has become clear that future molecular electronic, biomedical, and photonic systems will require the self-assembly of the associated device elements into a functional unit. One way to achieve this is to make use of the patterns that are produced by modulated systems, which can act as lithographic templates. In particular, spectacular long-range ordering on suitable length scales has been achieved with soft-condensed matter systems such as block copolymers, and related surface systems [29,30,55,56]. To date, the current patterns for templates are for the most part based on stripes and bubbles. Here, we show by means of simulations of a standard phase field model with Langevin dynamics [57–63] that a very much larger set of patterns may be produced. Most of these patterns are the result of a complicated mix of ordering mechanisms and instabilities that will require considerably more theoretical and experimental study before a detailed understanding is achieved. However, a subset of these patterns has already been found experimentally, in the context of ferrimagnetic garnet films as those studied by Molho and co-workers [10,11] and Seul and Wolfe [15,16], a fact that gives great confidence in the validity of the model. Ultimately, it is hoped that many of the patterns will be identified experimentally, and find their application as nanolithographic templates, thereby enriching the choice of patterns that are in current use.

In terms of the physics, the patterns discussed here are formed by taking the system through its complex free energy landscape, by means of successive quench trajectories inside the coexistence region of the phase diagram. The trajectories are chosen in such a way that the *topological constraints* of the system produce *strained* patterns, that need not evolve to the global free energy minimum of the system. These topological constraints arise from different aspects of the modulated system, and include factors such as a very high free energy barrier for the nucleation of stripes, the high bending stiffness of stripes, packing constraints imposed on the system by means of its initially ordered structure, etc. These factors conspire to make modulated systems very strongly *history* dependent, so that the *order* in which the different parameters are changed plays a crucial role in determining the patterns produced.

A short outline of this paper is as follows. In the next section, we discuss a minimal phase field model for modulated systems, which is based on the phenomenology of ferrimagnetic garnet films, as well as details of the simulations. Previously, this model has been extensively used to theoretically explore ordering and Ostwald ripening phenomena for systems quenched into the "hexagonal" or bubble phase (strictly speaking, a triangular lattice of cylindrical domains) [57–63]. Section III is used for a theoretical review. Section IV discusses some general features that we found for systems under strain. Section V discusses stripes under temperature-induced strain, including both *compressive* and *dilational* strain. Section VI describes the stripe-bubble transition (and

the lack of transition in the hard-wall regime). Section VII presents results for the hexagonal phase under strain. Throughout these sections, we show that the model both reproduces experimental patterns and predicts different patterns. Section VIII is reserved for a summary. Finally, we note that a brief summary of our main results has already been presented elsewhere [63].

II. MODEL AND SIMULATIONS

To generate the patterns in this work, we use an LRRI appropriate for ferrimagnetic garnet films. Most experiments performed on ferromagnetic films can be represented by a dipolar ferromagnet with uniaxial anisotropy in the geometry of a slab of finite thickness L and infinite extent in the plane. Strongly uniaxial films are required to avoid closure domains and branching in the wall structure. A standard phase field model for this system is given in terms of the order parameter $\psi(\mathbf{r},\tau)$ at spatial position $\mathbf{r}$ and time τ. Regions $\mathbf{r}$ where $\psi(\mathbf{r})>0$ represent spins pointing in the "up" direction (perpendicular to the slab), while regions with $\psi(\mathbf{r})<0$ represent spins pointing in the "down" direction. In our figures, regions with positive (negative) $\psi(\mathbf{r})$ are represented by a white (black) shading, respectively. The free energy functional $\mathcal{F}$ in dimensionless form [57,59] is

$$\mathcal{F}[\psi(\mathbf{r},\tau)] = \int d^2r \left[\frac{1}{2}(\nabla\psi)^2 + f(\psi) - H\psi \right] + \frac{\alpha}{2}\int\int d^2r\, d^2r'\, \psi(\mathbf{r}) g(|\mathbf{r}-\mathbf{r}'|)\psi(\mathbf{r}'). \quad (1)$$

In the first term, the $(\nabla\psi)^2$ gives the *lowest-order* approximation to the cost of creating a domain wall or interface, $f(\psi)$ is the local free energy, and $-H\psi$ is the linear coupling of the order parameter to the externally applied magnetic field H, oriented perpendicularly to the film. The local free energy has the standard temperature dependence associated with phase transitions: for temperature T greater than the critical temperature T_c, the local free energy has a single-well structure that represents the uniform phase; for $T<T_c$ (corresponding to our simulations) $f(\psi)=-1/2\psi^2+1/4\psi^4$, such that the minima associated with the resulting double-well structure correspond to each of the two coexisting phases. The double integral represents the LRRI, with the kernel given by

$$g(|\mathbf{r}-\mathbf{r}'|) = \frac{1}{|\mathbf{r}-\mathbf{r}'|} - \frac{1}{[|\mathbf{r}-\mathbf{r}'|^2+L^2]^{1/2}}, \quad (2)$$

as is appropriate for a ferromagnetic thin film. In the limit of very thin films, i.e., $L\to 0$, the kernel $g(|\mathbf{r}-\mathbf{r}'|)\to L^2/(2|\mathbf{r}-\mathbf{r}'|^3)$ becomes a purely repulsive dipolar potential. Such a system would be truly two dimensional, and have characteristics similar to an Ising model with dipolar interactions, as previously investigated by Stoycheva and Singer [64,65]. The relative strength of the LRRI is represented by the temperature-dependent parameter α. Throughout our discussions, we use α and T— somewhat loosely—as if the two were interchangeable. This is because both play very similar roles in regulating the characteristic length scales of the modulated phase (experimentally, α depends on T, but in a nontrivial, system-dependent way [15]). In our simulations, high-temperature, "shallow" quenches are mimicked by α's close to the critical $\alpha_c\approx 0.385$ (for $L=10$, in the deterministic zero-noise case) [59], while low-temperature, "deep" quenches are mimicked by values of α that are much smaller than α_c.

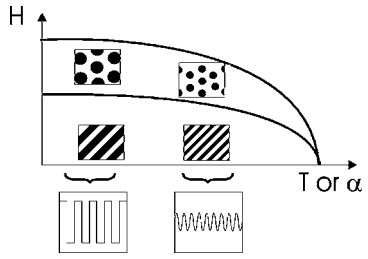

FIG. 1. Sketch of a phase diagram for a ferrimagnetic thin film. The phase diagram is symmetric with respect to the magnetic field H. First-order lines separate stripe, bubble, and homogeneous phases. The bubble phase is a low-density triangular lattice. Typical order parameter profiles illustrating the soft- and hard-wall regimes are also shown.

The time evolution of the system is given by the Langevin equation:

$$\frac{\partial\psi(\mathbf{r},\tau)}{\partial\tau} = -\frac{(-\nabla^2)^n}{2}\frac{\delta\mathcal{F}}{\delta\psi} + \sqrt{u}\zeta(\mathbf{r},\tau), \quad (3)$$

where $\zeta(\mathbf{r},\tau)$ represents the dimensionless thermal noise of strength μ, which is subject to the standard fluctuation-dissipation relation $\langle\zeta(\mathbf{r},\tau)\zeta(\mathbf{r}',\tau')\rangle=(-\nabla^2)^n\delta(\mathbf{r}-\mathbf{r}')\delta(\tau-\tau')$. The noise strength μ depends on the temperature and other parameters of the free energy as given, for example, in Eq. (9) in Ref. [59]. For a system with a *nonconserved* (*conserved*) order parameter, $n=0$ ($n=1$), respectively. In this work, we are focusing on patterns for ferrimagnetic garnet films, which corresponds to the $n=0$ case. This equation was then discretized on grids with sizes ranging from 256^2 to 512^2, and numerically integrated using standard pseudospectral methods with periodic boundary conditions [57–59].

The initial patterns for the simulations consisted of highly ordered stripe or bubble arrays, that were constructed with their proper, equilibrium wavelength characteristic of the given point of the phase diagram. These structures were then further equilibrated, in order to produce the equilibrium patterns. These were then used as initial conditions for the exploration of the patterns presented in this work, which were produced by means of subsequent quenches in α and H. Simulations were conducted both with and without noise; a further discussion of the role of noise is presented in Sec. IV.

III. THEORETICAL REVIEW

Figure 1 shows a sketch of the mean field phase diagram for the system as a function of the two parameters α and H. The phase diagram is symmetric with respect to H, with first-order transition lines separating the stripe, bubble, and

homogeneous phases. These phases are expected to meet at a ferromagnetic critical temperature T_c. In reality, the LRRI suppresses the fluctuations near T_c such that the onset of the modulated patterns occurs at a temperature that is somewhat lower than T_c [66]. For $H=0$, the stripe patterns are *symmetric*, with zero net magnetization. *Asymmetric* patterns result as H changes, since the stripes whose magnetization is parallel (antiparallel) to the field become wider (thinner), respectively. Above a critical value of H, there is a transition to an "hexagonal" phase consisting of cylindrical domains (the bubbles) arranged on a low-density triangular lattice. An important feature of the system is that at high α (or high T) the order parameter profile is a small-amplitude sinusoidal with a short period. This represents the so-called "soft-wall" regime. At low α (or low T), the order parameter profile resembles that of a "square-well" profile with a long period, which is the "hard-wall" regime.

Theoretical analyses of domain formation have been formulated by many authors in the past [4–9,12,13]. In principle, to obtain this equilibrium wavelength, one has to solve an infinite set of coupled equations in Fourier space [59], although considerable insight may be obtained with the single-mode approximation in the soft-wall regime or using a square wave for the hard-wall regime. For instance, for the soft-wall regime—described by the single-mode approximation—the period d of the lamellar patterns scales as $d \sim L^{1/3}$, while in the hard-wall regime $d \sim L^{1/2}$ [67]. The pattern period decreases with increasing temperature, since the LRRI predominate as the critical temperature point is approached, favoring the formation of more and more domain walls.

To understand the patterns formed, it is important to examine the relevant fluctuations for each of the phases and the ordering processes. In terms of the former, Garel and Doniach [9] and Sornette [12,13] showed that for the stripe phase, the effective elastic energy takes the form of a smectic-A free energy:

$$\mathcal{F} \approx \int d^2r \left[\frac{1}{2} B \left(\frac{\partial u}{\partial x} \right)^2 + \frac{1}{2} K \left(\frac{\partial^2 u}{\partial y^2} \right)^2 \right], \tag{4}$$

where the variable u represents the deviation of a domain wall from its equilibrium position (stripes are assumed to run along the y direction), and the compression modulus B and the curvature modulus K depend on α, L, and the equilibrium wave vector. This smectic free energy is anisotropic in its elastic response: transverse undulation modes (governed by the curvature term) are characterized by relatively low excitation energies, while the longitudinal compression modes require considerably higher energies. As a consequence, bending of stripes is favored over compression. Even in this case, magnetic stripes are characterized by a large bending stiffness [12,15], estimated to be about $\sim 10^3 kT_c$. This result is important, and accounts for the predominance of glassy states observed for ferrimagnetic systems, both experimentally [10,11,15,16] and in our simulations: except for temperatures close to T_c, temperature fluctuations simply do not play a role over most of the phase diagram. This implies that smectic positional correlations can have a macroscopic range in magnetic films at finite temperatures. For the bubble phase, the simplest effective elastic free energy is a two-dimensional isotropic energy [9], with a compressibility modulus and an isotropic shear modulus. The form of the free energy allows for a Kosterlitz-Thouless melting transition [68].

Analytical theories for melting in two dimensions predict that the profusion of topological defects in these systems destroys the long-range translational and orientational order. For two-dimensional modulated systems, the relevant topological defects are dislocations and disclinations. In the lamellar phase, disclinations of charge q are characterized by a mismatch of $2\pi q$ in the orientation angle after a lattice circuit. The characteristic disclinations are those with $q=1/2$ (the tip of a stripe) and $q=-1/2$ (a branching point with threefold rotation symmetry). These disclinations can be bound together in a dislocation, which is an extra row in an otherwise perfectly lamellar phase. In hexagonal phases, disclinations of charge q are characterized by a mismatch of $q\pi/3$ in the orientation angle after a lattice circuit [58,60]. The most common disclinations are those with $q=-1$ (a fivefold coordinated bubble) and $q=+1$ (a sevenfold coordinated bubble). A dislocation is a tightly bound pair of sevenfold and fivefold disclinations separated by one lattice spacing. Two-dimensional solids do not have long-range translational order: they are characterized by long-range orientational order and quasi-long-range translational order characterized by an algebraic decay of the translational correlation function. A second-order transition produced by the unbinding of dislocations leads to a phase characterized by short-range translational order (i.e., the exponential decay of the correlation function), and quasi-long-range orientational order. This intermediate phase is a nematic [69,70] for the stripe phase, and a hexatic [71–74] for the bubble phase. In particular, theory [69,75] predicts that the unbinding of dislocations in the hexagonal phase occurs at nonzero temperatures, while for the stripe phase it only occurs at $T=0$. However, smectic positional correlations have macroscopic range in magnetic films at $T>0$, and the predicted exponential decay of positional correlations is very difficult to assess [15]. Finally, another second-order transition produced by the unbinding of disclinations leads to the isotropic liquid phase. Another important feature in modulated phases is the presence of amorphous or glass phases, with abundance of topological defects [10,11,15,16]. These glassy phases fail to achieve long-range ordering, but may exhibit ordering on an intermediate length scale that goes beyond the first nearest-neighbor distance.

IV. ORDERED PATTERNS UNDER STRAIN

One of the goals of this work is to provide an understanding of the evolution of the initial highly ordered equilibrium patterns subject to temperature-induced or field-induced strain. For a given film thickness, the final patterns depend not only on α and H, but also on the *initial configuration*, i.e., whether it is stripe, bubble, or other, ordered or disordered, with the domains belonging to the majority or the minority phase, etc. In addition, because of the presence of topological constraints, modulated systems are strongly *his-*

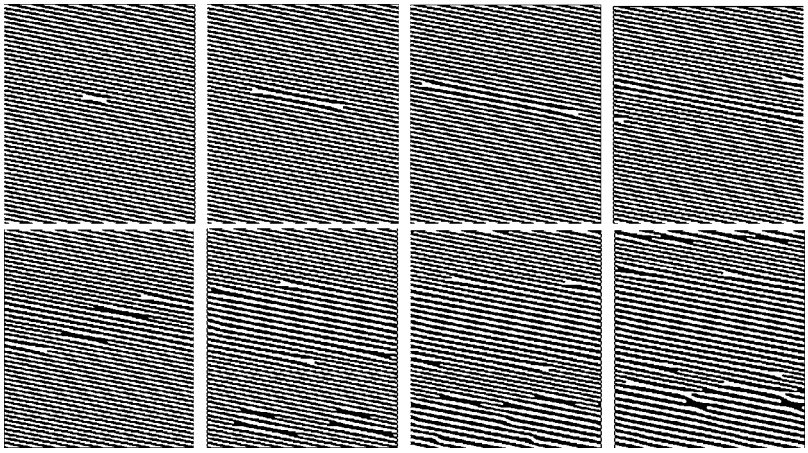

FIG. 2. Period adaptation of *symmetric* stripes under compressive strain by means of dislocation nucleation, climb, and stripe ejection for the direct quench $\alpha=0.34\rightarrow0.08$. Configurations are at times $\tau=100$, 500, 900, 1300 (top panels, left to right), and $\tau=1700$, 2500, 2900, and 3300 (bottom panels, left to right), respectively. Rectangular lattice of size 512^2.

tory dependent, so that *how* a specific point in phase space is reached is important. Many trajectories do not give the same patterns when the quench is reversed, and changes in α and H often do not commute. Initial and final values of α (or H) in the system may be linked through either a "direct" quench ($\alpha_i\rightarrow\alpha_f$), or through "stepwise" quenches with intermediate equilibration $\alpha_i\rightarrow\alpha_1\rightarrow\alpha_2\ldots\rightarrow\alpha_f$. This can lead to radically different configurations because of how the strain in the system is accommodated. Roughly, small strains like those produced by the stepwise trajectories allow for a better accommodation of strain, and this favors *affine* deformations. On the other hand, large strains, like those produced by the direct trajectories, pile up a considerable amount of strain on the patterns, and immediate release of the excess strain is achieved by the fragmentation of the domains or by the nucleation of domains within domains. There are innumerable ways of adding strain to modulated systems. We report primarily on cases when the system is either under *compressive* (too many domains) or *dilative* (too few domains) strain.

The topological constraints in the system arise from a variety of physical origins. For instance, there are very high free energy barriers for the nucleation of pairs of Bloch walls, a high bending stiffness for the stripes, packing constraints on the initial configurations—especially in the highly ordered configurations, that because of their symmetry leave "no room" for domains to escape, etc. As a result, the system is often precluded from reaching its final equilibrium pattern, and ends up in either a true metastable state or a kinetically frozen glassy state, that appears to be robust against small perturbations such as noise. There is therefore the expectation that experimentally these patterns may be stabilized, and ultimately become useful as templates. It is important to note that lack of noise does not necessarily imply zero temperature. For instance, for stripe patterns in ferrimagnetic films, experiments [10,11,14–16], and previous theoretical considerations [12,13] show that outside of the small critical region, temperature fluctuations are irrelevant and that the only role of temperature is to modulate the characteristic period. In the hexagonal phase, temperature fluctuations would be expected to modulate transitions to and from the hexatic phases. However, in magnetic garnet films the coercive friction associated with microscopic roughness effectively pins the bubbles, and thermal fluctuations are unimportant. Thus it is a standard technique in bubble memory technology to use an *ac* magnetic field superimposed on the *dc* field to simulate thermal motion. This is, for instance, the technique used by Seshadri and Westervelt [76,77] to study two-dimensional defect motion and a continuous hexatic-to-liquid melting transition as a function of bubble density. In these experiments, the *ac* field produces a breathing motion of the bubble whose radius undergoes a slight periodic expansion or contraction. This motion couples with substrate roughness originating from microscopic, random disorder on length scales shorter than the bubble radius. The net effect is an apparent random motion of the bubble.

V. STRIPES UNDER TEMPERATURE-INDUCED STRAIN

To understand the action of strain on the quenched patterns, consider a configuration of stripes at $H=0$. Let L_{lat} be the lateral dimensions of the film such that all the stripes are perpendicular to that side of the film. Let d_i be the equilibrium stripe period and N_i be the number of lamellae in the initial, perfect lamellar pattern, and let d_α and N_α be the corresponding stripe equilibrium period and equilibrium number at the final α after the quench. These must satisfy $L_{\mathrm{lat}}=N_i d_i=N_\alpha d_\alpha$, in equilibrium. Immediately after the quench, when the number of stripes is still the same, the strain produced by the quench in α is $\epsilon=(d_\alpha-d_i)/d_i$. When α is *decreased*, the equilibrium stripe period is larger and the number of stripes smaller. Hence, immediately after the quench, there is an excess number of stripes, and so the system is under *compressive* strain with $\epsilon>0$. The reverse situation is encountered if α is increased: after the quench, the number of stripes is lower than what is required for equilibrium, and the stripes are therefore under dilative, or extensional strain with $\epsilon<0$.

A. Stripes under compressive strain: Dislocation ejection

Consider an initial pattern of *symmetric* stripes ($H=0$) at high α (soft-wall regime with small period) quenched to a low α (hard-wall regime with large period). The system is under compressive strain, which is released by means of dislocation nucleation, dislocation climb, and stripe ejection [10–12], as shown in Fig. 2. The ejection of stripes allows the pattern to accommodate the increase in the stripe period induced by lowering α. In this process, the stripes shorten

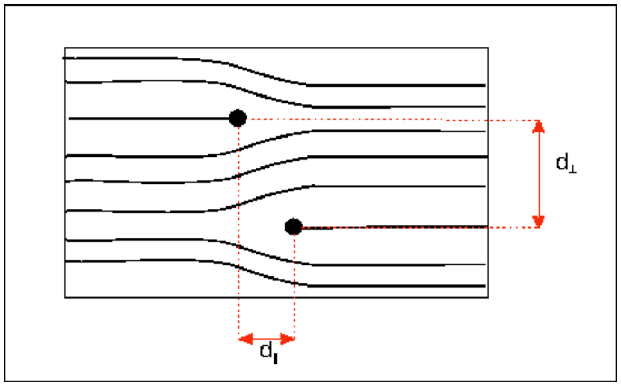

FIG. 3. (Color online) Sketch of two dislocations with opposite Burger's vector, with the parallel and perpendicular distances between the dislocation cores shown.

their length until they disappear rather than have their width go to zero. Purely strain-induced forces are seen in the earlier times, when dislocations are isolated. Dislocation interaction forces play a role when more dislocations are nucleated. The process of stripe ejection preserves the lamellar state during the coarsening process. The large change in α applied to the system in Fig. 2 allows for nucleation of several dislocations in both phases. Eventually, the tips of these dislocations separate incommensurate regions of different periods. This is clearly seen at times $\tau=2500$, 2900, where two regions of shorter period alternate with two regions having a larger period. These simulations reproduce some of the experimental observations by Seul and Wolfe [15,16] for symmetric stripes ($H=0$).

The dislocation ejection is facilitated by the Peach-Koehler force [78], which is a result from the strain-induced curvature of the stripes surrounding the dislocations. In addition to this force, the elastic interactions between dislocations are also important. If the dislocation lines are parallel to the layers of the smectic phase, the interaction force may be decomposed into its longitudinal component (i.e., oriented along the direction of the dislocations) and a perpendicular component [79]:

$$F_{\parallel} = \mathbf{b}_1 \cdot \mathbf{b}_2 \frac{B}{8(\pi\lambda)^{1/2}} \frac{d_{\parallel}}{d_{\perp}^{3/2}} \exp\left(-\frac{d_{\parallel}^2}{4\lambda d_{\perp}}\right),$$

$$F_{\perp} = \mathbf{b}_1 \cdot \mathbf{b}_2 \frac{B\lambda}{8(\pi\lambda)^{1/2}} \frac{1}{d_{\perp}^{3/2}} \left(1 - \frac{d_{\parallel}^2}{2\lambda d_{\perp}}\right) \exp\left(-\frac{d_{\parallel}^2}{4\lambda d_{\perp}}\right). \quad (5)$$

Here, $d_{\parallel}$ and $d_{\perp}$ are the parallel and perpendicular distances between dislocations (see Fig. 3); $\mathbf{b}_1$ and $\mathbf{b}_2$ are the Burger's vectors of the two dislocations; B is the elastic compression modulus; and λ is the penetration length [$\lambda=\sqrt{K/B}$, with K the smectic curvature elastic modulus in Eq. (4)]. These equations are valid for perpendicular separations considerably larger than the dislocation core. When the dislocations are on the same stripe line ($d_{\perp}=0$), the interaction becomes negligible. Note that the longitudinal component is attractive for dislocations with opposite Burger's vector, and repulsive when these are parallel. The sign of the perpendicular component, on the other hand, depends on the relative positions of the two dislocations. The longitudinal force is responsible for dislocation climb, and adds to the strain-induced force (proportional to $B\epsilon$). The perpendicular component provides a mechanism for the clustering of dislocations, thereby leading to the formation of a domain wall or grain boundary.

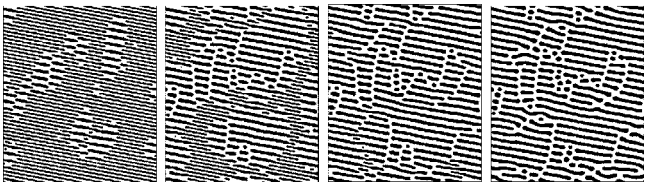

FIG. 4. Ordering of an *asymmetric* stripe pattern under compressive strain after a quench $\alpha=0.34\rightarrow0.08$ at constant field $H=0.08$. Left to right panels show configurations at times $\tau=1800$, 2000, 2200, and 4000, respectively. Rectangular lattice of size 512^2.

Interesting patterns emerge for *asymmetric* ($H\neq0$) stripes subject to a temperature quench. Here, in addition to the Peach-Koehler force and the dislocation interaction, there is an additional force which derives from the action of the magnetic field on the dislocation core. Qualitatively, this may be understood as follows [12]. Let $d_+(d_-)$ represent the width of the stripes whose magnetization is parallel (antiparallel) to the magnetic field. The curvature of the dislocation core is $\sim 2/d_{+(-)}$. If σ denotes the surface tension of the wall, then the Laplace pressure on the dislocation core is $2\sigma/d_{+(-)}$. In the presence of a magnetic field when d_+ increases and d_- decreases, this implies a decreased Laplace pressure for "+" dislocations and an increasing pressure for "−" dislocations. In other words, the excluding force decreases with increasing H for "+" dislocations thereby pulling them in, and facilitates the ejection of the "−" dislocations (see, for instance, Fig. 9).

For very small fields, the process of stripe ejection under a temperature quench looks qualitatively similar to that for the $H=0$ stripes. For slightly higher field, the phenomenology changes. For instance, Fig. 4 shows period adaptation of asymmetric stripes when α is decreased under a constant field $H=0.08$. The normal process of stripe ejection has been replaced by *segment coarsening*. This process is initially triggered around $\tau=1700$, by the formation of two dislocation pairs separated by a single stripe, that now *thickens* in the region surrounded by the gaps left by the dislocations. This is a highly correlated process, with the thickened region of stripes inducing the pinching of neighboring stripes. Eventually, incommensurate domains of thick and thin stripes appear between times $\tau=1800$ and 2000. Thin domains disappear by shortening their length. At $\tau\approx2200$, all segments have achieved the same "period": regions of perfectly parallel segments are now separated from each other by either bubbles or by arrays of segment heads, thereby forming grain boundaries. Nearby segment regions may be viewed as "terraces"; the segments of two neighboring terraces occupy alternating positions, with bubbles mediating the readjustment of the period.

B. Stripes under dilative strain: Transverse instabilities and topological defects

We now consider stripes systems under dilational strain, i.e., the patterns obtained when α is increased from a low to

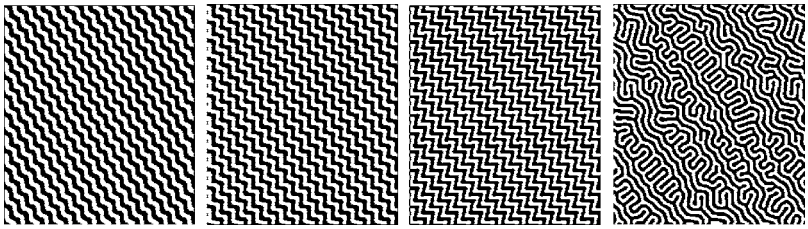

FIG. 5. Final configurations for *symmetric* stripe patterns under dilative strain by means of stepwise quenches, starting from a configuration at $\alpha=0.08$ that was quenched successively to $\alpha=0.10$, 0.12, 0.16, and 0.18 (left to right panels). Rectangular lattice of size 512^2.

a high value. In principle, to release the strain, N_α needs to increase through the nucleation of additional stripes in order for the system to remain in the lamellar phase. However, the large energetic barriers to the nucleation of pairs of Bloch walls preclude this process. Instead, the excess dilative strain is reduced by means of an undulation or buckling instability, which arises from a competition between the elastic extensional energy and the opposing elastic bending energy [80,81].

First, we consider the case of symmetric stripes. After a threshold of dilative strain is reached, the stripes undergo a senoidal undulation deformation, which involves the collective buckling of lamellae on macroscopic scales. Stabilized configurations for different values of α are shown in Fig. 5. The undulation pattern for $\alpha=0.10$ becomes a stabilized "deep" undulation pattern (involving higher harmonics) for $\alpha=0.12$. For higher values of dilative strain, strong nonlinear behavior leads to the formation of chevron or zigzag patterns. One such stabilized configuration is observed for $\alpha=0.16$. The curvature walls of the initial undulation give way to the discontinuity walls of the chevron pattern, characterized by a slope discontinuity. Experimentally, it has been observed that the transverse period of the chevron structure undergoes adjustment via the expulsion of "metadislocations" through climb [15]. The simulations need systems larger than the ones presented in this work to observe this phenomenon.

After a second threshold of dilative strain, the chevron pattern "melts" via nucleation of disclination dipoles that originate in the tips of the patterns. For symmetric stripes, an equal number of such pairs emerges for each of the phases. The last panel of Fig. 5 shows a nearly frozen configuration for $\alpha=0.18$, with the time evolution shown in Fig. 6. The early times ($\tau=400$ and 800) show the emerging dipoles, which are aligned perpendicularly to the original lamellar patterns and emerge at angles of 120° with respect to the original walls of the chevron structure. This process of line branching (or pincement in the liquid crystal literature) relieves strain by adding additional lamellae. Interestingly, if a dipole emerges at the tip of a discontinuity profile in a given layer, the discontinuity profile in the nearest-neighbor layer towards which the dipole is pointing does not nucleate a disclination dipole but becomes smoothly curved, acting like a "cap" to the disclination dipole in the first layer. The maximum number of dipoles occurs for $500<\tau<1500$; at later times many of these dipoles are actually re-absorbed. This process creates arrays of disclination pairs separated by relatively smooth stripes. These observations are in excellent agreement with the experimental observations of Seul and Wolfe [15,16], except that the simulation results are characterized by a higher density of disclination dipoles because of their higher strains.

As for symmetric stripes, we have examined the asymmetric case quenching successively from $\alpha=0.08\rightarrow0.12\rightarrow0.14\rightarrow0.16$. For example, Fig. 7 shows the time evolution for the quench $\alpha=0.14\rightarrow0.16$ ($H=0.10$). The amplitude of the initial undulation patterns increases with time, and eventually leads to the nucleation of disclination pairs in the majority phase. However, this process is different from the corresponding symmetric case process. There, the disclination pairs grow out of the discontinuity of the chevron pattern. For the asymmetric stripes, these discontinuities are never observed: the undulation grooves in the minority black phase become more "square," with larger amplitudes, while others become more triangular with a smaller amplitude. The net result may be interpreted as the nucleation of disclination pairs in the majority (in this case the white) phase, without having really gone through the chevron structure, or the pincement process. As time evolves, the low-amplitude triangular grooves become smoother, and flatten out while the black

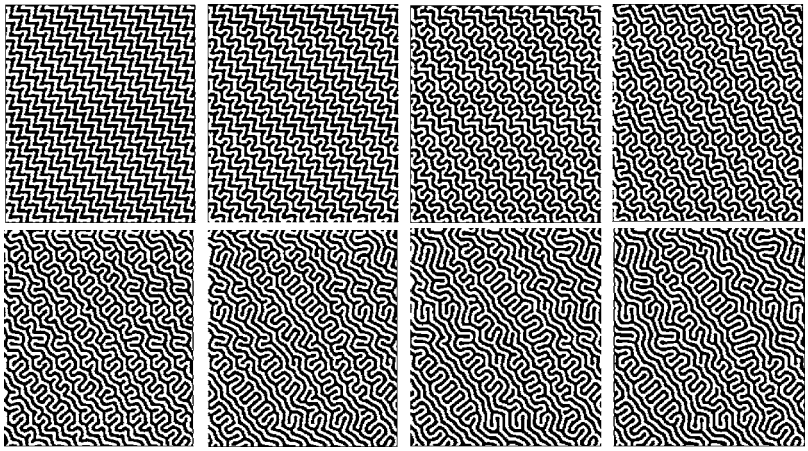

FIG. 6. Time evolution of a symmetric chevron pattern melting after a quench $\alpha=0.16\rightarrow0.18$. Configurations for times $\tau=400$, 800, 1600, 5000 (top panels, left to right) and $\tau=9000$, 19 000, 33 000, 47 000 (bottom panels, left to right) are shown. Rectangular lattice of size 512^2.

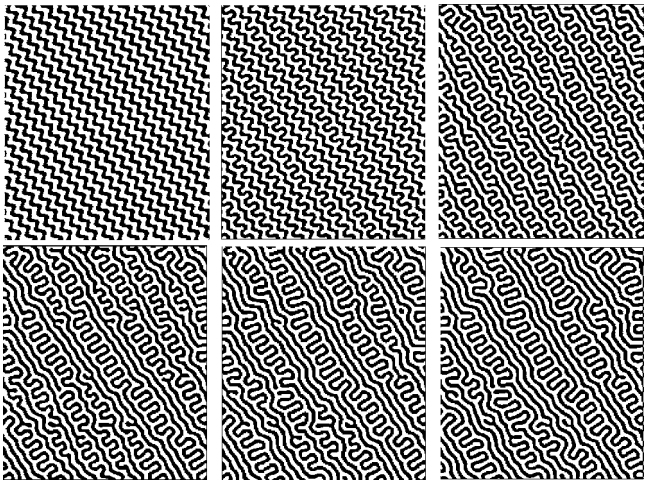

FIG. 7. Time evolution of an asymmetric chevron pattern at constant field $H=0.10$ melting after a quench $\alpha=0.14\rightarrow0.16$. Configurations for times $\tau=0$, 2500, 4500 (top panels), 13 000, 25 000, 37 000 (bottom panels) are shown. Rectangular lattice of size 512^2.

square profiles keep growing in amplitude (or alternatively, the white disclination pairs keep growing in length). The minority (black) phase also nucleates disclination dipoles, but these are much fewer than those in the majority (white) phase. These disclination dipoles, however, do originate through the line branching or pincement process. During the entire processes, the magnetization stays constant.

VI. FIELD QUENCH FOR CONSTANT α: STRIPE-BUBBLE TRANSITION AND FIELD-INDUCED STRAIN

Stripe-bubble transitions in ferrimagnetic films may be induced by varying the H field. Starting from a symmetric stripe pattern, and then uniformly increasing H, the width d_+ of the stripes with magnetization parallel to the field increases, while the antiparallel stripe width d_- decreases. For weak fields, the sum d_++d_- stays constant, and equal to the initial stripe period. At higher fields, d_- decreases slowly and attains a limiting value, while d^+ continues to increase and diverges near complete saturation. As a consequence, the total period must also diverge in this limit. For higher field, there are therefore two possible scenarios. First, to increase the period with H, some of the d_- stripes must disappear. This can take place through the process of dislocation nucleation and ejection [10–12], as previously described for temperature-induced strain (Sec. V A). This process is not reversible: once the stripes have been ejected, bringing the field back to $H=0$ does not recover the initial pattern, since the cost of nucleating Bloch wall pairs is simply too high. In complete analogy with the case of temperature-induced strain, when the field is brought back to zero, the patterns are under dilative strain and undergo the undulation and chevron instabilities, as well as the nucleation of disclination dipoles if the strain is large enough.

As a second alternative, another deformation mode involving inhomogeneous variations of the stripe thickness may take place. These "peristaltic" modes give rise to the necking instability. Theoretically, this may be understood through a modification of the smectic-A free energy to include these modes [13]. The resulting effective free energy then takes on the form of a lyotropic liquid crystal, with a third elastic modulus. If the width of the minority stripes falls below a certain threshold [4], the stripe domains become unstable with respect to variations in their thickness. This appears as a pinching or strangling of the stripes, which signals the onset of the stripe-to-bubble transition. It results in the complete rupture of the stripes that collapse into bubbles. This process is completely reversible: the fusion of bubbles into stripes under a decreasing field is also known as the "stripe-out" instability.

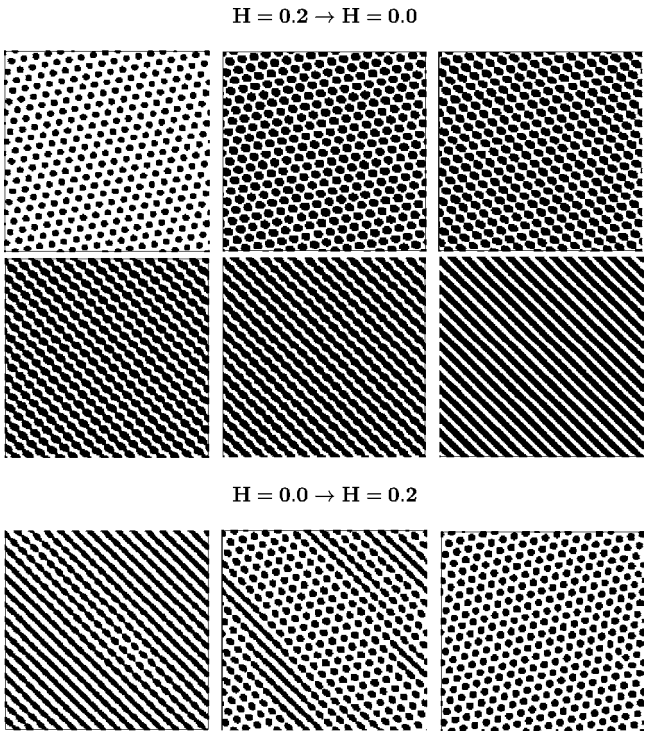

FIG. 8. Top panels: time evolution of the soft-wall ($\alpha=0.34$) "stripe-out" instability as $H=0.20\rightarrow0.0$. Configurations at $\tau=0$, 200, 250, 300, 350, and 1000 are shown. Bottom panels: time evolution for the reverse transition ($H=0.0\rightarrow0.2$) at $\tau=1000$, 1200, and 3000. Note the presence of the peristaltic modes. Square lattice of size 256^2.

In our simulations, we have observed both of these strain accommodation modes, albeit in different regimes. In the high-α or "soft-wall" regime, the peristaltic modes preempt the nucleation of dislocations, and the reversible stripe-bubble transition is observed as shown in Fig. 8. For low temperatures, the hard-wall profile of the domains precludes both the peristaltic and stripe-out instabilities. Considering a stripe pattern for $H\neq0$, if a dislocation is introduced into an otherwise perfect stripe pattern, then the process of strain accommodation by means of stripe ejection takes place as illustrated in Fig. 9, and no transition to bubbles is observed.

Field quenches involving hard-wall triangular arrays of bubbles do not change the fundamental geometry of the quenched pattern, unless very large changes are involved. For instance, as shown in Fig. 10, quenching the hexagonal

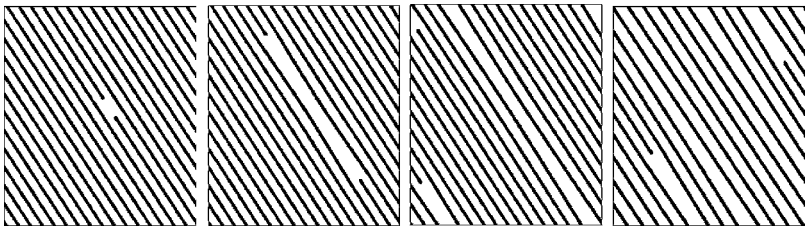

FIG. 9. Time evolution of a hard-wall stripe pattern quenched from $H=0.0\rightarrow0.25$ at constant α. This figure illustrates again the dislocation climb and ejection as the mechanism for period adjustment. Configurations at time $\tau=300$, 2200, 4500, and 13 000 are shown. Rectangular lattice of size 512^2.

phase from $H=0.15\rightarrow0$ just leads to an increase in the size of the black bubbles, without any shape transformation. A further decrease in the field to $H=-0.15$ results in an unexpected configuration, where the bubble domains form the *majority* phase (the equilibrium configuration is the negative of the first panel of Fig. 10—minority phase of white bubbles on a black majority background). Increasing the field still further to $H=-0.22$ brings about a radical change, and ultimately results in the formation of small white bubbles on a perfect honeycomb lattice. Further increases in the field result in the uniformly saturated phase.

These changes are completely reversible, provided they do not involve shape transformations. Thus increasing the field again from $H=-0.15$ to 0.15 recovers all of the previous configurations. However, when shape changes have taken place, new configurations result. Thus when the honeycomb configuration is quenched from $H=-0.22$ to -0.15, a frozen, disordered bubble phase is obtained. When the $H=-0.22$ configuration is rapidly quenched to $H=0.0$ (i.e., omitting the intermediate quench), a configuration of "fat" bubbles is obtained, that is similar to the very initial configuration, except that the phases are now inverted! A further quench to $H=0.15$ also produces a hexagonal phase of majority bubbles. From the symmetry of the quenches, if we take this $H=0.15$ configuration, and successively apply $H=0.15\rightarrow+0.22\rightarrow0.0\rightarrow0.15$, we would recover the very initial pattern shown in Fig. 10. We have checked that these results are robust against small noise [82].

VII. HEXAGONAL BUBBLE PATTERNS UNDER STRAIN

In this section, we discuss the behavior of the hexagonal bubble patterns under dilative strain. In all cases, we start from final, metastable, or frozen patterns at low temperatures ($\alpha=0.08$), obtained in the previous section through field quenches, and then take the system to successively higher values of α, at constant field H. Here, truly interesting patterns emerge. Some simply represent temporal configurations as part of the time evolution, while others emerge as long-lived metastable or frozen patterns. We begin the presentation with a summary of the "final" patterns obtained from the simulations in absence of noise, followed by a discussion of how this "kinetic" map is altered by the presence of noise. After this, a more detailed discussion of the time evolution of some individual runs is presented. It is convenient to introduce a shorthand notation to describe the different quenches in this section. The notation $S:12\rightarrow15$ will indicate a stepwise quench from $\alpha=0.12$ to $\alpha=0.15$; $D:08\rightarrow34$ will indicate a direct quench from $\alpha=0.08$ to $\alpha=0.34$, etc.

Although we found a number of very interesting patterns under dilative strain—especially when the initial configurations themselves were nonequilibrium patterns, like bubbles in the majority phase—we found that compressive strain did not produce "unexpected" results: mainly the original bubbles disappeared or coalesced to make room for the correct period of the equilibrium pattern. Here therefore we only report the results pertaining to dilative strain.

Bubble patterns under dilative strain: A"kinetic" map of the patterns

Figure 11 shows a kinetic map of the final patterns obtained for initial bubble patterns and then subjected to dilative strain by increasing α. The initial bubble patterns are those obtained for $\alpha=0.08$ and comprise *equilibrium* lattices, where the domains belong to the *minority* phase ($H=0.25$ and $H=0.15$), and *strained* lattices, where the domains be-

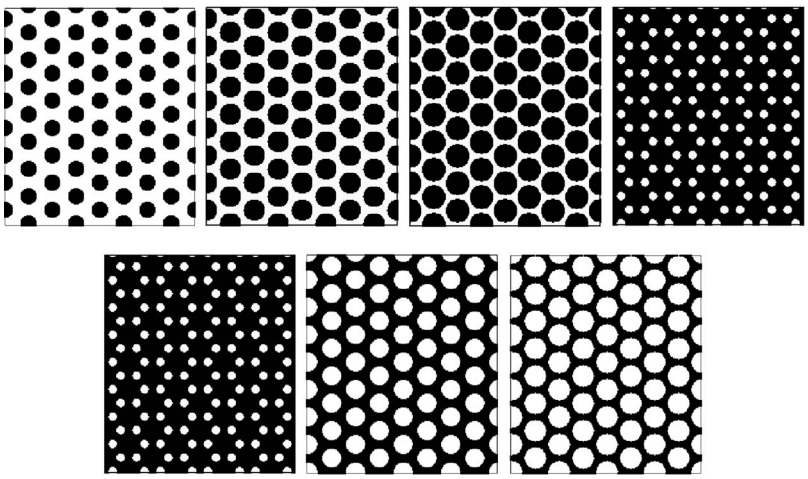

FIG. 10. Final configurations obtained after stepwise quenches in H at constant $\alpha=0.08$. Top panels at $H=0.15\rightarrow0.0\rightarrow-0.15\rightarrow-0.22$. Bottom panel shows the reverse quenches $H=-0.22\rightarrow0.0\rightarrow0.15$. Interestingly, the intermediate step $H=-0.22\rightarrow-0.15$ (not shown) produces a disordered bubble lattice. Rectangular lattice of size 256^2.

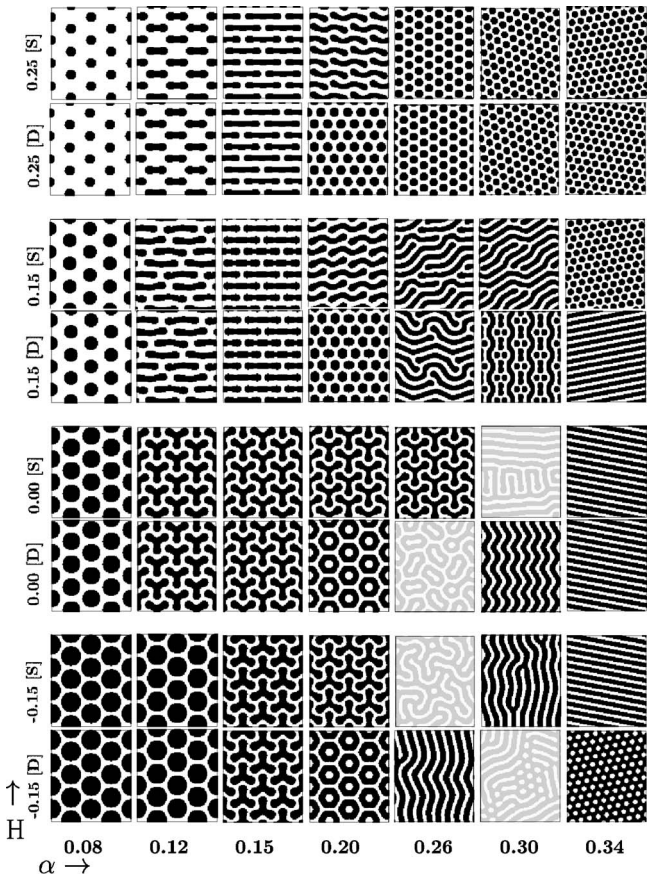

FIG. 11. Final patterns as obtained by means of temperature-induced dilative strain on initial triangular lattices at different values of H, with α increased from left-to-right in either a stepwise $[S]$ or direct $[D]$ quench. All the configurations in the $[D]$ quenches are obtained througth a direct quench starting from the left-most $\alpha=0.08$ configuration. The $[S]$ configurations are obtained from the closest configuration to the left that presents an ordered array of domains. This generally means the configuration immediately to the left, except for the following exceptions: $H=0.15$ and $H=-0.15$, the configurations for $\alpha=0.20$ are the initial configurations for $\alpha=0.26$, 0.30, and 0.34; $H=0.0$, the configuration for $\alpha=0.26$ is the initial configuration for $\alpha=0.30$ and 0.34. All configurations are effectively frozen, except those marked in grey that are evolving slowly. For ease of visualization, the configurations have been cut to show only one-fourth of the simulation cell, of size 256^2.

long to the *majority* phase ($H=0.0$ and $H=-0.15$). The latter were obtained through field quenches as described in Sec. VI. Results for the $H=-0.22$ case (a honeycomb lattice of the minority phase) are not shown, since all the quenches starting from this configuration end up in the equilibrium hexagonal lattice (of white minority domains on a black background). In Fig. 11, the stepwise quenches are marked with an S, while the direct quenches are marked with a D. Stepwise trajectories generally indicate that a given configuration is obtained from the immediately preceding one. This is always the case when the latter is a well-ordered configuration with a distinctive symmetry; however, if that is not the case, the "initial" configuration for the stepwise trajectory is taken to be the last ordered configuration. For instance, for $H=-0.15$ each configuration at the left is the initial pattern for the next configuration at the right until $\alpha=0.20$; the configurations for $\alpha=0.26$ and 0.30 are relatively disordered and therefore the configuration at $\alpha=0.20$ is taken as the initial one for all $\alpha=0.26$, 0.30, and 0.34. These cases are specified in the figure caption.

Roughly speaking, the patterns fall into four regimes, based on the final value of α.

(i) *Low temperature* $0.08 \leqslant \alpha \leqslant 0.165$ *regime.* Domains of the *minority* phase experience an elliptical instability, and end up as ordered lattices of either "dumbbell" or rounded segments. Domains in the *equal* or *majority* phase experience a higher-harmonic shape transition, and end up as "Y" shapes with trigonal symmetry. As α increases, the center of the Y domain becomes thinner, and the tips become more rounded. In all cases, the patterns are independent of whether the quench was stepwise or direct.

(ii) *Low-intermediate temperature* $0.165 \leqslant \alpha \leqslant 0.220$ *regime.* The final configurations here depend very much on whether the quench has been stepwise or direct. Domains of the minority phase are wavy segments if the trajectory has been stepwise, or form hexagonal bubble lattices if the quench has been direct. *Equal or majority phase* domains, under a larger dilative strain, acquire the Y shape in stepwise trajectories, or form ring patterns under a direct quench. In both cases the domains form a triangular lattice.

(iii) *High-intermediate temperature* $0.22 \leqslant \alpha \leqslant 0.31$ *regime.* Configurations here all depend upon whether stepwise or direct quenches have been involved. Domains in the *minority* phase for high fields ($H=0.25$) end in the equilibrium hexagonal configuration. For all the other field values, there is a wide variety of patterns, generally consisting of glassy states of melted stripes, stripe segments, and bubbles, all in various proportions. Some of these patterns seem to have stabilized over time, while others (indicated by the gray shading) are still evolving. This slow evolution is explained by the fact that for this range of parameters there is a crossover between the regime where (generally nonequilibrium) structures are completely frozen [(i) and (ii)] to the regime where patterns quickly evolve to the equilibrium configuration in (iv).

(iv) *High temperature* $0.31 \leqslant \alpha \leqslant 0.36$ *regime.* Here, in the high-α, soft-wall regime, domains have higher mobilities and mostly reach their equilibrium configuration. It is interesting that the points $(\alpha, H)=(0.34, \pm 0.15)$ correspond to the stripe-bubble coexistence region, and stepwise or direct quench trajectories determine whether the final configuration is a lamellar phase or a triangular lattice.

Now we consider how this kinetic map is modified by the presence of temperature fluctuations, i.e., random noise. The configurations with the domains in the *minority* phase seem to be quite robust to the presence of small noise [82]. The only exception for $H=0.25$ is that the bubble lattices in the high temperature regime are not "perfect" but have some topological defects. For $H=0.15$ two configurations are not stable: the quench $D:08 \rightarrow 30$, ends in a mixture of bubbles and stripes, although the time evolution is very similar to that for the zero-noise case; and the quench $D:08 \rightarrow 34$, which ends in an equilibrium stripe-bubble coexistence pattern. In addition, in the quench $D:08 \rightarrow 15$, the segments are disordered.

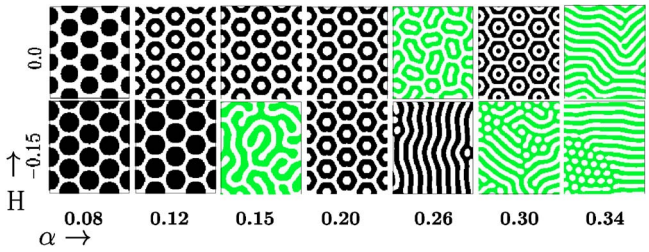

FIG. 12. (Color online) Final patterns as obtained by means of temperature-induced dilative strain on initial triangular lattices of majority domains under random noise. Direct and stepwise trajectories seem to produce the same final configurations. Black configurations are effectively frozen while grey configurations are evolving slowly. For ease of visualization, the configurations have been cut to show only one-fourth of the simulation cell, of size 256^2.

The configurations with the domains in the *majority* phase seem to be quite more sensitive to noise, which can be explained by the fact that these domains are subject to considerably more strain than the domains in the minority phase. In particular, the Y shape seems to be unstable to noise and these configurations cannot be obtained from quenches from $\alpha=0.08$ to $\alpha=0.12$ or $\alpha=0.15$. If, however, one takes a lattice of Y shapes as the initial lattice, some trajectories are recovered. For $H=0.0$, these are $S:15\rightarrow 20$, $S:26\rightarrow 30$, and $S:26\rightarrow 34$ (but not $S:20\rightarrow 26$); for $H=-0.15$ these are $S:15\rightarrow 20$, $S:20\rightarrow 26$, $S:20\rightarrow 30$. If the Y shapes cannot be obtained from the the fat bubbles on the left, then what are the shapes that can be obtained under the presence of noise? In Fig. 12, we present results for domains in the majority phase under dilative strain and noise. We find that stepwise and direct trajectories give approximately the same results, and therefore this figure only has two rows corresponding to each value of the field. For $H=0.0$ the ring shape preempts the Y shape obtained under zero noise; and the rings are remarkably stable. For $\alpha=0.26$, the rings slowly start to melt, similar to what happens in the quench $D:08\rightarrow 26$ under zero noise. Interestingly, for $\alpha=0.30$ a new configuration is stabilized under noise; $\alpha=0.34$ is evolving towards the equilibrium stripe phase. For $H=-0.15$ the fat bubbles evolve by initially undergoing the Y shape instability, but these lattices are not stabilized; only a direct quench to $\alpha=0.20$ produces stable rings. Quenches to $\alpha=0.26$ produce senoidal stripes, and to $\alpha=0.30$ and 0.34, the equilibrium stripe-bubble coexistence.

1. Bubble patterns under dilative strain: Time evolution

Having gained an overview of the final patterns that are formed in the simulations, we briefly consider their time evolution. In general, the stepwise quenches involve affine deformations, at least for lower α, while the direct quenches lead to rapid fragmentation of the original domains, maybe followed by their reconstitution in different shapes over a longer period of time.

The top two rows in Fig. 13 show the time evolution of domains undergoing a quench $S:08\rightarrow 12$ without noise. The domains in the minority phase $H=0.25$, first row) undergo an initial elliptical instability and they finally stabilize in "dumbbell" shapes at approximately $\tau\simeq 1800$ (total running time was $\tau=15\,000$). The domains in the majority phase ($H=0.0$, second row) present harmonic shape distortions that take the morphology through the "apple" shape at $\tau=1800$ and triangular fingering instability to a final configuration of perfectly triangular symmetric Y shapes that stabilize at $\tau\simeq 4000$ (total running time was $\tau=20\,000$). Interestingly, the configurations for higher α's stabilize in this pattern of perfectly triangular symmetric Y shapes earlier. For instance, $\alpha=0.20$ stabilizes at $\tau\simeq 1000$ while $\alpha=0.26$ stabilizes at $\tau\simeq 100$. The Y shape becomes unstable for higher values of α. The third row shows a direct quench $D:08\rightarrow 15$ under noise.

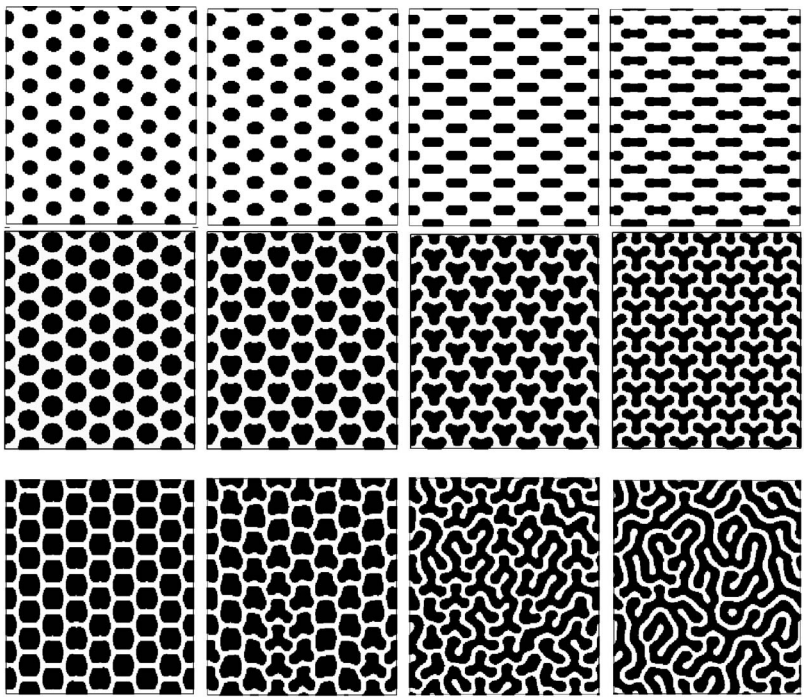

FIG. 13. Top two rows show the time evolution of domains undergoing a stepwise quench $\alpha=0.08\rightarrow 0.12$ without noise. First row: domains in the minority phase ($H=0.25$) at times $\tau=400$, 700, 1000, and 1800. Second row: domains in the majority phase ($H=0.0$) at times $\tau=0$, 1800, 2000, and 4000. The third row shows the time evolution of majority domains ($H=-0.15$) under a direct quench $\alpha=0.08\rightarrow 0.15$ with noise. Times shown are $\tau=1400$, 2150, 2900, and 4900. Rectangular lattice of size 256^2.

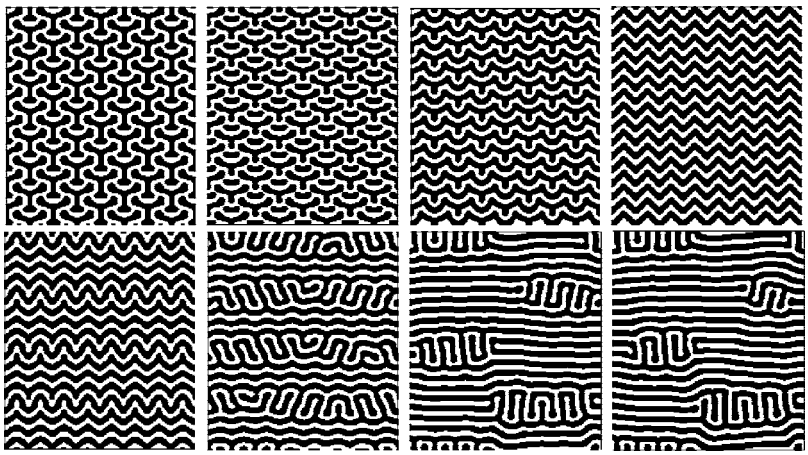

FIG. 14. Time evolution for a Y-shape lattice of majority domains ($H=0.0$) for a dilative quench $\alpha=0.26\rightarrow0.30$. Times shown are $\tau=800$, 1200, 1400, 2200 (first row) and $\tau=5500$, 6500, 16 000, and 26 000 (second row). Rectangular lattice of size 256^2.

A lattice of Y domains is no longer stable, but the domains initially undergo the triangular fingering instability, as can be seen at times $\tau=2150$ and 2900.

Figure 14 shows a particularly interesting case of shape instabilities undergone by the Y -shaped domains (under zero noise) when subjected to further dilative strain in the quench $S:26\rightarrow30$ ($H=0.0$). The Y shapes fatten at the tips, and become thinner in the center, ultimately fragmenting there. The deformed arms then reconnect forming a chevron pattern (clearly visible at $\tau=2200$) with nucleation of disclination pairs as shown at $\tau=5500$ and 6500. The configuration evolves very slowly and eventually reaches the *equilibrium* stripe pattern. The time evolution for a quench $S:26\rightarrow34$ (not shown) is much faster; by $\tau=2500$ the system has reached the perfect stripe phase. The intermediate stages in the melting of the Y lattice depend on the final value of α but are independent of the initial Y lattice (i.e., all the configurations for $H=0.0$ and $\alpha=0.12$ to $\alpha=0.26$ give the same time evolution when quenched to a higher α.)

Figures 15–19 show the time evolution following different direct quenches without noise. Some of the intermediate patterns are quite exotic and unanticipated, with many interesting intermediate stages before the final pattern is reached. For instance, Fig. 15 shows the formation of two bubble lattices, following a quench from $\alpha=0.08$ (first panel in Fig. 10) to $\alpha=0.20$ (first row) and $\alpha=0.34$ (second and third rows). The transformation here is initiated by the nucleation of a sublattice of white rings surrounding the initial black bubbles. Immediately after that, fragmentation of the black background takes place. For the direct quench $D:08\rightarrow20$, this gives intermediate six-point starred shapes ($\tau=30$) which rapidly break to form the bubble lattice. For $D:08\rightarrow34$, there is a *tertiary* nucleation of white domains ($\tau=30$) whose growth eventually cuts up the black background ($\tau=100$). At $\tau=900$ there is a curious configuration of serpentine stripes alternating with rows of bubbles, before the system reaches the equilibrium hexagonal bubble lattice. Figure 16 shows the quench $D:08\rightarrow26$, that gives undulat-

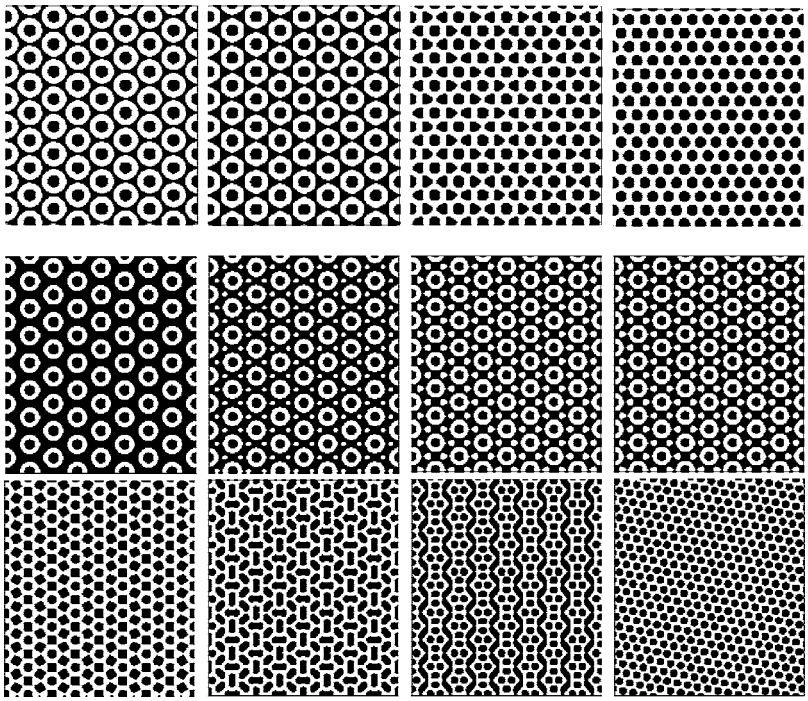

FIG. 15. Time evolution for two direct quenches of initial minority bubbles at $H=0.25$. Top row: direct quench $\alpha=0.08\rightarrow0.20$. Times shown are $\tau=10$, 30, 40, 100. Bottom rows: direct quench $\alpha=0.08\rightarrow0.34$. Times shown are $\tau=10$, 30, 60, and 80 (second row) and $\tau=100$, 600, 900, and 1400 (third row). Rectangular lattice of size 256^2.

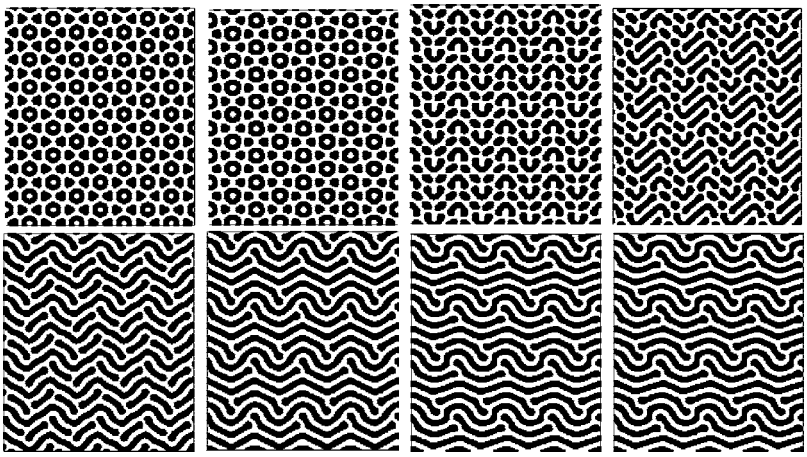

FIG. 16. Time evolution for the direct quench $\alpha=0.08\rightarrow0.26$ at $H=0.15$. Times shown are $\tau=100$, 3400, 4200, and 4600 (top row) and $\tau=7000$, 11 000, 13 000, and 29 000 (bottom row). Rectangular lattice of size 256^2.

ing stripes lines alternating with undulating stripe segments. Careful examination of the patterns reveals that the continuous lines are either zigzag patterns of smaller amplitude or more senoidal-like patterns of higher amplitude. These continuous lines are separated by rows of stripe segments that "travel" in one direction in a row, and in the opposite direction in the next row. The structure does not change from $\tau=13\,000$ to $\tau=29\,000$ but it is not clear if it is "frozen."

The rings that form in the majority phase, either with or without noise, appear very early in the time evolution ($\tau\leqslant100$) by nucleation of a sublattice of white bubbles within the original majority black bubbles; and remain stable (for simulation times $\tau\simeq25\,000$). For higher α, they tend to become more hexagonal. Figure 17 shows the time evolution for direct quenches at $H=0.0$ where the rings are no longer stable, but appear as an early configuration in the time evolution. The first row is a quench $D:08\rightarrow26$, which shows slow melting of the rings. The second and third rows show the quench $D:08\rightarrow30$, where the early-time rings evolve to an intermediate configuration of alternating stripes and rows of bubbles ($\tau=200$). The stripes have a senoidal modulation which in turn modulates the bubbles. Thus going up a column of bubbles, thick and thin bubbles alternate: thick bubbles are flanked by convex modulations of the stripes, while thin bubbles are flanked by concave modulations of the surrounding stripes (they are "squeezed"). From $\tau\simeq450$ to $\tau\simeq1700$ the system shows perfect stripes. However, they do not have the equilibrium period and are under dilative strain; the system then undergoes a senoidal instability as described in Sec. V B, finally stabilizing in a chevron structure. Another trajectory that develops early-time hexagonal rings is shown in Fig. 18, that shows a direct quench $D:08\rightarrow26$ at $H=-0.15$. We observe similar modes of evolution as those in Fig. 17. In particular, the configuration at $\tau=600$ is similar to that observed at $\tau=200$ in Fig. 17: undulating stripes separate rows of bubbles. Within these rows, thick and thin bubbles alternate, the thin bubbles being squeezed by the flanking stripes. Between $\tau\simeq1100$ and $\tau\simeq3700$ the configu-

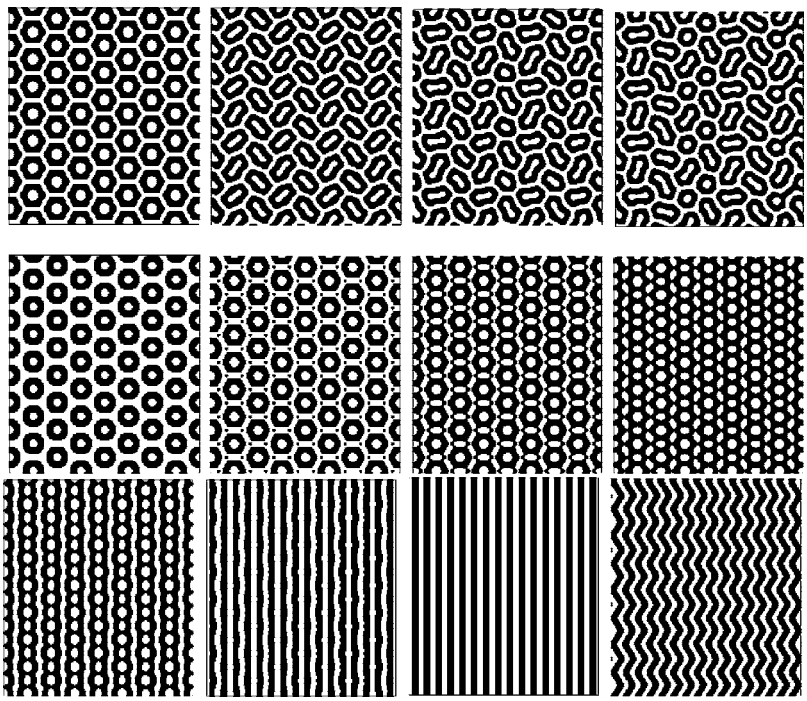

FIG. 17. Time evolution for two direct quenches of initial minority bubbles at $H=0.0$. Top row: direct quench $\alpha=0.08\rightarrow0.26$. Times shown are $\tau=100$, 4000, 12 000, and 32 000. Bottom rows: direct quench $\alpha=0.08\rightarrow0.30$. Times shown are $\tau=10$, 20, 30, and 100 (second row) and $\tau=200$, 300, 500, and 3500 (third row). Rectangular lattice of size 256^2.

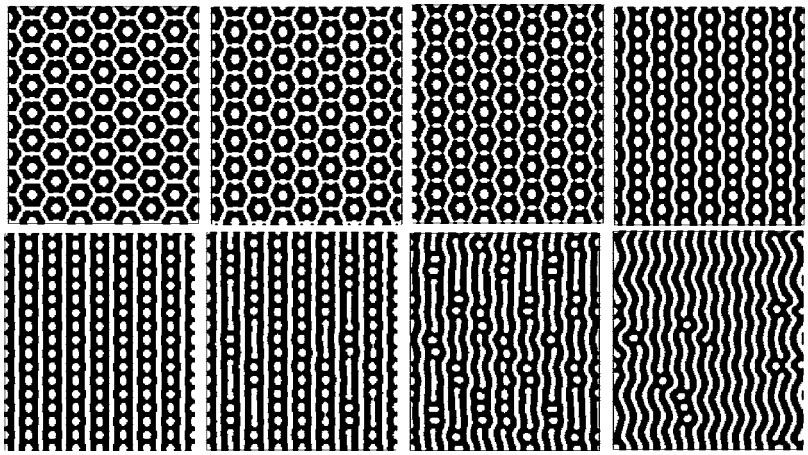

FIG. 18. Time evolution for the direct quench $\alpha=0.08\rightarrow0.26$ at $H=-0.15$. Times shown are $\tau=250$, 500, 550, and 600 (top row) and $\tau=1100$, 5300, 6100, and 17 700 (bottom row). Rectangular lattice of size 256^2.

ration remains the same. After that, bubbles start to come together in short stripes as shown for $\tau=5300$. For $\tau=38\,000$ (not shown) all but three bubbles have disappeared; the configuration is expected to end in a senoidal pattern. This time evolution is independent of whether the initial configuration is that of fat bubbles at $\alpha=0.08$, $H=-0.15$, or that of rings obtained in $D:08\rightarrow20$, $H=-0.15$ (see Fig. 11). A quench to $\alpha=0.34$, however, strongly depends on the initial configuration since the equilibrium configuration for $\alpha=0.34$ and $H=\pm0.15$ is very close to the stripe-bubble coexistence. This was shown in Fig. 11, where the quench $S:20\rightarrow34$ (initial lattice of Y shapes) gave a perfect stripe lattice, while a quench $D:08\rightarrow34$ (initial lattice of fat bubbles) gave a perfect triangular lattice. This dependence on the initial configuration is further illustrated in Fig. 19, where the first row shows the quench $D:08\rightarrow34$ (initial lattice of fat bubbles) while the second and third rows show a quench $D:20\rightarrow34$ (initial lattice of rings). The quench $D:08\rightarrow34$ ends in a perfect hexagonal lattice of bubbles that stabilizes at $\tau\simeq2200$ while the quench $D:20\rightarrow34$ ends in a stripe configuration (except for dislocations). In presence of noise all the configurations for $\alpha=0.34$ and $H=\pm0.15$ end in the equilibrium stripe-bubble coexistence.

In summary, the time evolution of these quenched modulated systems is characterized by strain-induced instabilities, that give rise to complex morphology based on the nucleation of opposite-phase bubbles inside domains, domain fragmentation, the coexistence of serpentine stripes and bubbles, etc. It may well be that these kinds of transient patterns will prove to be useful experimentally. The key issue here is the long-time stabilization of these patterns, which may presumably be achieved by means of kinetic freezing.

2. Hexagonal bubble patterns under dilative strain: More field quenches

For completeness, we also considered quenches of the final configurations shown in Fig. 11, and subjected them to further quenches in the magnetic field, while keeping the

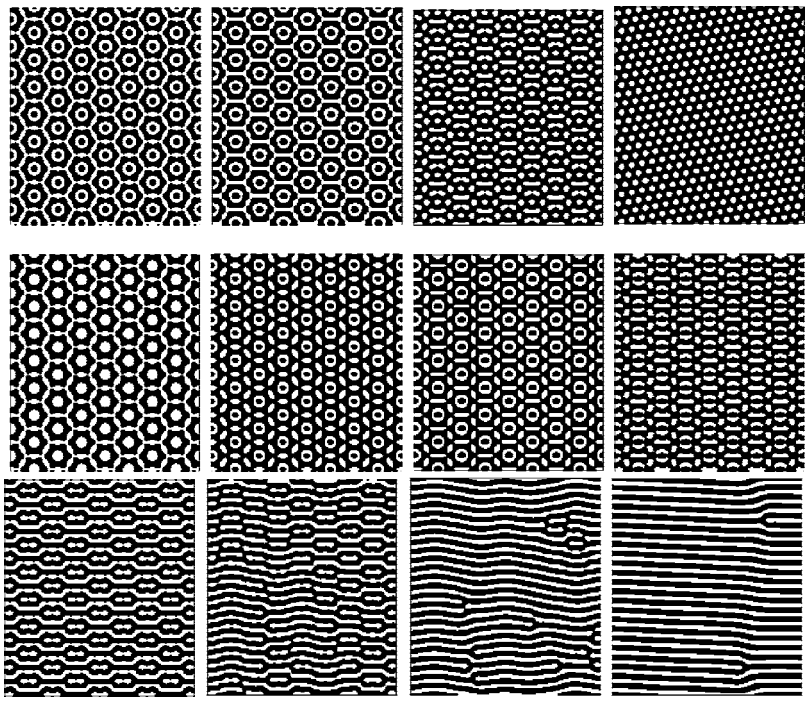

FIG. 19. Time evolution for two direct quenches of domains at $H=-0.15$. Top row: direct quench $\alpha=0.08\rightarrow0.34$. Times shown are $\tau=100$, 500, 700, and 2200. Bottom rows: direct quench $\alpha=0.20\rightarrow0.34$ (initial lattice of rings). Times shown are $\tau=50$, 100, 250, and 350 (top row) and $\tau=500$, 2500, 3100, and 17 500 (bottom row). Rectangular lattice of size 256^2.

value of α fixed. The results fall into three basic regimes:

(i) *High temperature* $0.31<\alpha<0.35$ *regime*. Variations in H lead to transitions between stripe and bubble patterns, as previously discussed. Even when a very large change in the field is applied, e.g., from $H=0.25\rightarrow-0.25$, the equilibrium lattice is obtained very fast, with intermediate stripe and shape transitions of the type already discussed. Given the soft-wall nature of this regime, this result is easily anticipated.

(ii) *High-intermediate temperature* $0.22\lesssim\alpha\lesssim0.31$ *regime*. Since in this regime some of the final configurations generally do not have a regular periodic geometry, involve some measure of disorder, and/or are still evolving [since the regime is a crossover between (i) and (ii)], we do not consider these configurations.

(iii) *Low and low-intermediate temperature* $0.08\lesssim\alpha<0.22$ *regimes*. Starting from the ring shapes for initially negative and zero H values, and then increasing the field in steps of 0.10 or 0.15, we find that the ring shapes turn out to be very robust persisting all the way to $H=0.35$. Patterns based on Y -shaped domains are also robust, but less so than the rings. They stay in the Y shape until $H<0.25$; at $H=0.25$ they become fragmented into alternating dumbbells and bubbles and finally at $H=0.30$ they become an equilibrium hexagonal bubble lattice. Finally, we consider the straight segments of $\alpha=0.15$ and the wavy segments of $\alpha=0.20$ at positive fields: when the field is brought to zero, these end in straight and senoidal stripes, respectively. Adding a negative field does not break the stripes because these values of α produce a relative hard-wall profile and the stripes become stable. An example of these quenches for $\alpha=0.20$ is presented in Fig. 20. An interesting contrast is presented on Fig. 11, where moving up and down the column (i.e., looking at different values of the field) corresponding to $\alpha=0.20$ shows very different configurations.

Finally, the evolution of these patterns under field quenches, including the Y -shaped lattices, are robust against small amplitude noise, and follow the patterns described.

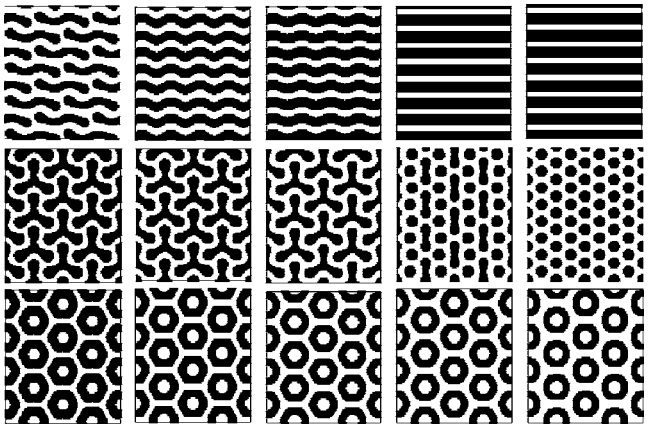

FIG. 20. Final configurations for different stepwise field quenches, where each configuration on the left represents the initial configuration for the next panel on the right. All the configurations are for $\alpha=0.20$. First row: field values are $H=0.25$, 0.0, −0.15, −0.25, and −0.30. Second and third row: field values are $H=$ −0.15, 0.0, 0.15, 0.25, and 0.30. For ease of visualization, the configurations have been cut to show only one-fourth of the simulation cell, of size 256^2.

VIII. SUMMARY

In summary, we have explored—by means of large-scale simulations—the complex morphology of modulated systems by means of a reliable phase field model. This model faithfully reproduces the experimental and theoretical results in previously explored regions of the phase space. However, by tuning the strain in the system—by means of temperature and field quenches—one is able to take the system into different metastable or glassy configurations, that to date have largely been unexplored. These patterns are stabilized by the large topological constraints present in the system, which preclude the system from reaching its true equilibrium patterns. As the system is quenched, there is clear evidence of strain-induced instabilities that are strongly history dependent. It is hoped that the patterns explored in our simulations will ultimately be realized experimentally, and perhaps prove to be technologically useful as nanoscale templates for application purposes. In this regard, our simulations are probably most true to ferromagnets which are characterized by very high elastic modulii. It remains an open question that we aim to explore in the future whether these patterns are robust for other fluid and soft-condensed matter systems.

ACKNOWLEDGMENTS

We gratefully acknowledge financial support from NSF Grant No. CAREER-0348039, DOE Grant No. DE-FG-02-98ER45685, and an Army Research grant.

[1] See, for example, J. D. Gunton, M. San Miguel, and P. Sahni, in *Kinetics of First Order Phase Transitions*, Phase Transitions and Critical Phenomena, Vol. 8, edited by C. Domb and J. Leibowitz (Academic Press, London, 1983).
[2] M. Seul and D. Andelman, Science **267**, 476 (1995).
[3] C. Bowman and A. C. Newell, Rev. Mod. Phys. **70**, 289 (1998).
[4] C. Kooy and U. Enz, Philips Res. Rep. **15**, 729 (1960).
[5] A. A. Thiele, J. Appl. Phys. **41**, 1139 (1970).
[6] W. F. Druyvesteyn and J. W. Dorleijn, Philips Res. Rep. **26**, 11 (1971).
[7] J. A. Cape and G. W. Lehman, J. Appl. Phys. **42**, 5732 (1971).
[8] J. A. Cape, J. Appl. Phys. **43**, 3551 (1972).
[9] T. Garel and S. Doniach, Phys. Rev. B **26**, 325 (1982).
[10] P. Molho, J. Gouzerh, J. C. S. Levy, and J. L. Porteseil, J. Magn. Magn. Mater. **54-57**, 857 (1986).
[11] P. Molho, J. L. Porteseil, Y. Souche, J. Gouzerh, and J. C. S. Levy, J. Appl. Phys. **61**, 4188 (1987).

[12] D. Sornette, J. Phys. (Paris) **48**, 151 (1987).
[13] D. Sornette, J. Phys. (Paris) **48**, 1413 (1987).
[14] M. Seul, L. R. Monar, L. O'Gorman, and R. Wolfe, Science **254**, 1616 (1991).
[15] M. Seul and R. Wolfe, Phys. Rev. A **46**, 7519 (1992).
[16] M. Seul and R. Wolfe, Phys. Rev. A **46**, 7534 (1992).
[17] Y. Yafet and E. M. Gyorgy, Phys. Rev. B **38**, 9145 (1988).
[18] A. O. Tsebers and M. M. Maiorov, Magnetohydrodynamics (N.Y.) **16**, 21 (1980).
[19] A. O. Tsebers, Magnetohydrodynamics (N.Y.) **17**, 113 (1981).
[20] R. E. Rosensweig, M. Zahn, and R. Shumovich, J. Magn. Magn. Mater. **39**, 127 (1983).
[21] T. Mitsui and J. Furuichi, Phys. Rev. **90**, 193 (1953).
[22] B. S. Kwak *et al.*, Phys. Rev. Lett. **68**, 3733 (1992).
[23] R. M. Weis and H. M. McConnell, Nature (London) **310**, 47 (1984).
[24] R. M. Weis and H. M. McConnell, J. Phys. Chem. **89**, 4453 (1985).
[25] M. Lösche and H. Möhwald, Eur. Biophys. J. **11**, 35 (1984).
[26] D. Andelman, F. Brochard, and J.-F. Joanny, J. Chem. Phys. **86**, 3673 (1987).
[27] H. Möhwald, Annu. Rev. Phys. Chem. **41**, 441 (1990).
[28] H. M. McConnell, Annu. Rev. Phys. Chem. **42**, 171 (1991).
[29] S. O. Kim *et al.*, Nature (London) **424**, 411 (2003).
[30] W. A. Lopes and H. M. Jaeger, Nature (London) **414**, 735 (2001).
[31] J. V. Selinger, Z. G. Wang, R. F. Bruinsma, and C. M. Knobler, Phys. Rev. Lett. **70**, 1139 (1993).
[32] F. J. Bartoli *et al.*, Phys. Rev. E **58**, 5990 (1998).
[33] J. V. Selinger, J. Xu, R. L. B. Selinger, B. R. Ratna, and R. Shashidhar, Phys. Rev. E **62**, 666 (2000).
[34] S. Zhang, E. M. Terentjev, and A. M. Donald, Eur. Phys. J. E **11**, 367 (2003).
[35] C. A. Murray and D. H. Van Winkle, Phys. Rev. Lett. **58**, 1200 (1987).
[36] C. A. Murray and R. A. Wenk, Phys. Rev. Lett. **62**, 1643 (1989).
[37] C. A. Murray, W. O. Sprenger, and R. A. Wenk, Phys. Rev. B **42**, 688 (1990).
[38] S. Leibler and D. Andelman, J. Phys. (France) **48**, 2013 (1987).
[39] T. Baumgart, S. T. Hess, and W. W. Webb, Nature (London) **425**, 821 (2003).
[40] M. Rappolt *et al.*, Biophys. J. **84**, 3111 (2003).
[41] S. J. Marrink, A. H. de Vries, and A. E. Mark, J. Phys. Chem. B **108**, 750 (2004).
[42] S. Rozovsky, Y. Kaizuka, and J. T. Groves, J. Am. Chem. Soc. **127**, 36 (2005).
[43] F. Haenssler and L. Rinderer, Helv. Phys. Acta **40**, 659 (1967).
[44] R. P. Huebener, *Magnetic Flux Structures in Superconductors* (Springer-Verlag, Berlin, 1979).
[45] S. Mori, C. H. Chen, and S.-W. Cheong, Nature (London) **392**, 473 (1998).
[46] Q. Ouyang and H. L. Swinney, Nature (London) **352**, 610 (1991).
[47] K. R. Elder, J. Viñals, and M. Grant, Phys. Rev. Lett. **68**, 3024 (1992).
[48] K. R. Elder, J. Viñals, and M. Grant, Phys. Rev. A **46**, 7618 (1992).
[49] M. C. Cross and D. I. Meiron, Phys. Rev. Lett. **75**, 2152 (1995).
[50] A. Plass, J. A. Last, N. C. Bartelt, and G. L. Kellog, Nature (London) **412**, 875 (2001).
[51] K. O. Ng and D. Vanderbilt, Phys. Rev. B **52**, 2177 (1995).
[52] J. R. Thomsen, W. Cowan, M. J. Zuckermann, and M. Grant, in *Proceedings of the XVIII Winter Meeting On Statistical Physics Ozxatepo Mexico, 1989*, edited by A. E. Gonzalez, C. Varea, and M. Medina-Noyola (World Scientific, Singapore, 1989).
[53] N. Sulitanu and F. Brinza, Mater. Sci. Eng., B **106**, 155 (2004).
[54] Y. Lu *et al.*, Nature (London) **410**, 913 (2001).
[55] M. Park *et al.* Science **276**, 1401 (1997).
[56] C. Park, J. Yoon, and E. L. Thomas, Polymer **44**, 6725 (2003).
[57] C. Roland and R. C. Desai, Phys. Rev. B **42**, 6658 (1990).
[58] C. Sagui and R. C. Desai, Phys. Rev. Lett. **71**, 3995 (1993).
[59] C. Sagui and R. C. Desai, Phys. Rev. E **49**, 2225 (1994).
[60] C. Sagui and R. C. Desai, Phys. Rev. Lett. **74**, 1119 (1995).
[61] C. Sagui and R. C. Desai, Phys. Rev. E **52**, 2807 (1995).
[62] C. Sagui and R. C. Desai, Phys. Rev. E **52**, 2822 (1995).
[63] C. Sagui, E. Asciutto, and C. Roland, Nano Lett. **5**, 389 (2005).
[64] A. D. Stoycheva and S. J. Singer, Phys. Rev. E **64**, 016118 (2001).
[65] A. D. Stoycheva and S. J. Singer, Phys. Rev. E **65**, 036706 (2002).
[66] S. A. Brazovskii, Zh. Eksp. Teor. Fiz. **68**, 175 (1975) Sov. Phys. JETP **41**, 85 (1975).
[67] W. A. Barker and G. A. Gehring, J. Phys. C **16**, 6415 (1983).
[68] J. M. Kosterlitz and D. J. Thouless, J. Phys. C **6**, 1181 (1973).
[69] D. R. Nelson and J. Toner, Phys. Rev. B **24**, 363 (1981).
[70] D. R. Nelson and R. A. Pelcovits, Phys. Rev. B **16**, 2191 (1977).
[71] B. I. Halperin and D. R. Nelson, Phys. Rev. Lett. **41**, 121 (1978).
[72] D. R. Nelson and B. I. Halperin, Phys. Rev. B **19**, 2457 (1979).
[73] D. R. Nelson and B. I. Halperin, Phys. Rev. B **21**, 5312 (1980).
[74] A. P. Young, Phys. Rev. B **19**, 1855 (1979).
[75] J. Toner and D. R. Nelson, Phys. Rev. B **23**, 316 (1981).
[76] R. Seshadri and R. M. Westervelt, Phys. Rev. B **46**, 5142 (1992).
[77] R. Seshadri and R. M. Westervelt, Phys. Rev. B **46**, 5150 (1992).
[78] See, for example, M. Klemen, *Points, Lines and Walls* (Wiley, New York, 1983).
[79] S. Chandrasekhar, *Liquid Crystals* (Cambridge University Press, Cambridge, England, 1992), Chap. 5.
[80] N. A. Clark and R. B. Meyer, Appl. Phys. Lett. **22**, 493 (1973).
[81] R. Ribotta and G. Durand, J. Phys. (Paris) **38**, 179 (1977).
[82] For the simulations with noise we simply used the Euler integration scheme which when applied to Eq. (3) reads $\psi(\mathbf{r},\tau+\delta\tau)=\psi(\mathbf{r},\tau)-\delta\tau\, 0.5(\delta\mathcal{F}/\delta\psi)+\mu'\,\zeta(\mathbf{r},\tau)$ where $\mu'=\delta\tau\sqrt{\mu}$. We used as time integration $\delta\tau=0.01$. We considered as "small noise" values of μ' that are 1% or less of the amplitude of the order parameter in the particular regime.